PCCP

PAPER

View Article Online
View Journal

Cite this: DOI: 10.1039/d6cp00849f

UV photo-uncaging of Ru(II)-polypyridyl bioconjugates in high vacuum

Marcel Strauss,†[b] Yong Hua,†[a] Michael Pfeffer,[a] Alfredo Di Silvestro,[a] Philipp Geyer,[b] Marcel Mayor,[a] Markus Arndt*[b] and Valentin Köhler*[a]

Received 7th March 2026,
Accepted 10th June 2026

DOI: 10.1039/d6cp00849f

rsc.li/pccp

Ruthenium(II) polypyridyl complexes exhibit rich photophysics that, in solution, have been widely exploited in chemical applications ranging from catalysis to ligand release. Here, we extend this concept to the gas phase by investigating photo-uncaging and charge-state control of $[(tpy)(acac)RuL]^{n+/-}$ complexes, where the leaving moiety L are simple pyridine derivatives – with or without a charged group – and pyridines conjugated to polypeptide cargoes such as insulin. We find that sequential absorption of two photons at 355 nm or 266 nm can drive efficient ligand loss. In the absence of solvent stabilization and under the high photon fluences accessible in molecular beam experiments, photo depletion becomes highly efficient, enabling practical optical manipulation relevant to mass spectrometry, gas-phase photochemistry, and molecular quantum optics.

Introduction

Photocleavage in solution is an active field of research that promises advances in, *e.g.*, drug delivery and activation, and the manipulation of cellular signaling.[1–7] Photochemistry in high vacuum is complementary to that, and being unperturbed by any solvent allows for different reaction pathways and dynamics. In the absence of any medium, intermolecular ligand substitution and proton transfer, or solvent-assisted charge stabilization, are impossible. Instead, the molecule can dissipate energy through vibrational relaxation, radiative decay, structural rearrangement, and fragmentation.

Many reaction channels can be explored in tandem mass spectrometry, where an analyte ion is selected prior to depletion of the parent molecule, and the appearance of fragments is studied under irradiation by intense ultraviolet light.[8–10] Photodissociation in the gas phase[8–17] can differ substantially from photochemistry in solution. Experiments with peptide anions linked to a nitrobenzyl ether with a 3,5-bis(trifluoromethyl)-phenoxy leaving group were found to release a phenolate ion in vacuum, while similar compounds in solution tended to dissociate a protonated leaving group. Interestingly, in high vacuum, the peptides approximated solution-like behavior when the number of amino acid residues was increased.[16] In another example, a bodipy-meso-methyl-pyridinium ion was found to dissociate poorly in solution, while it efficiently cleaved in high vacuum where reversible charge transfer was suppressed.[17] Using appropriate tags, fragmentation and molecular charge reduction can be achieved at various wavelengths. The attachment of a bodipy-pyridinium motif facilitated the charge reduction of RNAse and lysozyme conjugates by green light at 532 nm,[17] while nitrobenzyl ethers (NBE) with charged leaving groups enabled efficient neutralization of an insulin conjugate at 266 nm.[15] In these studies, the fragment yields increased with increasing charge on the parent molecule, indicating that the electrostatic repulsion between the charged protein and the departing photocage favors their dissociation. Consistent with this finding, dissociative ionization by heterolytic cleavage has not been observed so far. It would require the photon energy to both break the chemical bond and separate opposite charges. This raises the question of whether a repulsive charge between the photocage and the biomolecule can facilitate photocleavage at lower charge states.

Here, we investigate Ru–pyridyl complexes, which have already been extensively studied in solution[18–25] where they undergo efficient intersystem crossing from the excited state to a long-lived triplet metal-to-ligand charge transfer state. We have selected terpyridine–acetylacetonato–ruthenium $[Ru(tpy)(acac)(py)]^+$ (**1**) as a motif[19,26–28] that carries a monodentate pyridine ligand as a possible leaving group. This motif has a sizable absorption cross-section in the ultraviolet range, where high power laser sources are readily accessible. Derived compounds are reasonably stable and can be further diversified synthetically. Compound **1** and related compounds have also been reported to show minimal or no ligand exchange upon irradiation in solution in a single photon process,[29] while we find efficient dissociation of

[a] University of Basel, Department of Chemistry, St. Johanns-Ring 19, CH-4056, Basel, Switzerland. E-mail: valentin.koehler@unibas.ch
[b] University of Vienna, Faculty of Physics, VCQ & VDSP, Boltzmanngasse 5, A-1090, Vienna, Austria. E-mail: markus.arndt@univie.ac.at
† These authors contributed equally to this work.

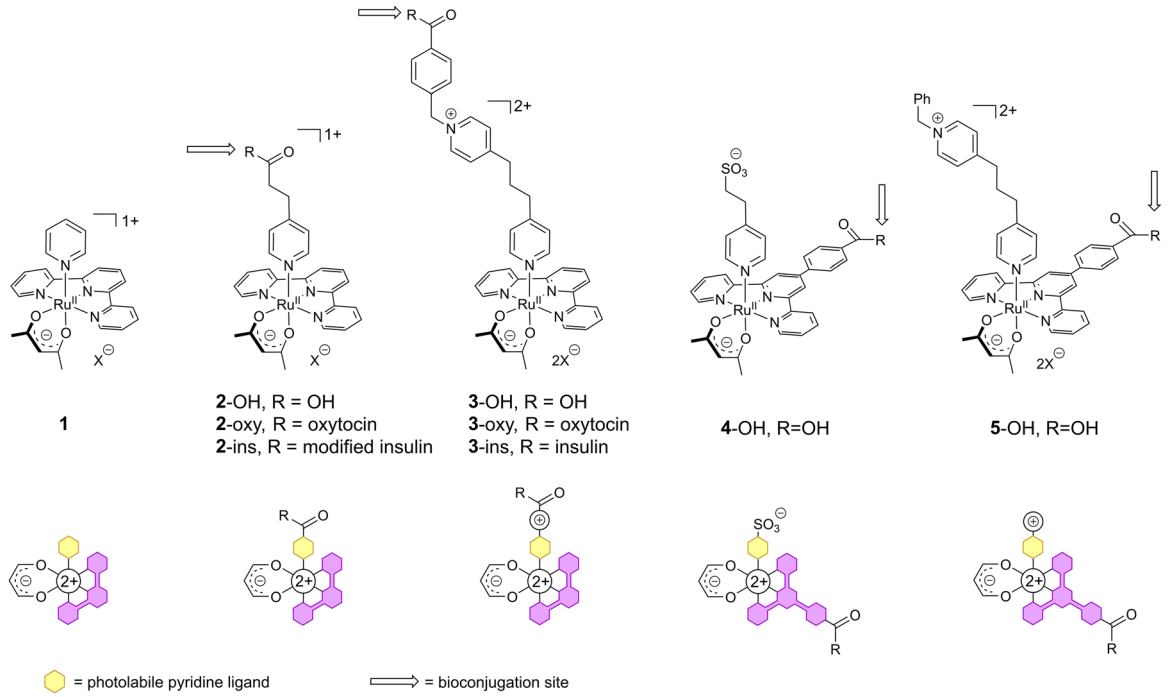

Fig. 1 Terpyridine–acetylacetonate–ruthenium complexes for UHV Photolysis. [(tpy)(acac)RuL]^{n} ions were studied as photocleavable tags for polypeptides in the gas phase. The central motif **1** carries a single positive charge. Installation of a functionalized linker in the para-position of the monodentate pyridine ligand in **2** provides a handle for bioconjugation, indicated by an arrow. In **3**, a pyridinium cation is introduced to promote photolysis *via* Coulomb repulsion with the positively charged ruthenium core. Compounds **2** and **3** were evaluated individually as well as linked to oxytocin and insulin. Compounds **4** and **5** are intended for bioconjugation *via* the tightly bound tpy moiety. This design allows to remove either a negative charge in negative ion mode (**4**) or a positive charge in positive ion mode (**5**), respectively. The colored cartoon structures at the bottom have been included for a clear presentation of the structural elements and hence the design intention behind the individual structures.

compounds **2–5** in high vacuum in a two-photon process. Fig. 1 shows the core motif **1** which carries an overall positive single charge. A functional handle can be installed on the leaving pyridine group for the bioconjugation of compound **2**. To probe the possibility of charge-promoted cleavage, we additionally introduce a pyridinium unit into the linker of complex **3**. Assuming point charges are located at the ruthenium center and at the nitrogen atom of the pyridinium unit, we estimate a repulsive Coulomb energy of about 100 kJ mol^{-1} (*ca.* 1 eV) if the propylene linker is fully extended. A positively charged pyridinium unit close to the surface of the conjugated biomolecule may also help direct the positively charged ruthenium complex away from the biomolecule, thereby reducing unwanted solvation effects of the biomolecule on the photocage.

The compounds were synthesized and characterized as described in the supplementary information (SI) and introduced into a Waters Q-TOF Ultima tandem mass spectrometer by electrospray ionization. Molecular ions were mass-selected with a quadrupole filter and subsequently irradiated with a 4.5 ns (FWHM) laser pulse at either 355 nm (3.49 eV) or 266 nm (4.66 eV). 355 and 266 nm, respectively, are conveniently accessible wavelengths within the absorption profile of the compounds and do not necessarily coincide with their absorption maxima. The near-flat-top laser beam ($r_L \sim 1.9$ mm) delivered pulse energies of up to 5 mJ at 355 nm and 1.8 mJ at 266 nm. The laser was aligned counter-propagating to the ion beam and timed to interact with a short segment of the ion packet before injection into the time-of-flight mass spectrometer (TOF-MS). The repetition rate was set to 10 Hz to ensure single-pulse excitation of each molecule.

Photodissociation pathways are obtained from the resulting tandem mass spectra by monitoring how laser excitation depletes the parent ion and populates fragment channels. In parallel, the extent of dissociation is quantified by the parent survival ratio S/S_0, where S is the integrated parent–ion signal recorded with the laser on and S_0 is obtained under otherwise identical conditions with the laser blocked. Survival curves are measured as a function of photon fluence Φ and analyzed using a sequential-absorption model,[16]

$$\frac{S}{S_0} = 1 - \alpha + \alpha(1 + \gamma\sigma_{PD}\Phi)e^{-\sigma_{PD}\Phi} \quad (1)$$

In this parametrization, σ_{PD} is the photodepletion action cross section at the excitation wavelength and sets the characteristic fluence scale for depletion. The prefactor α represents the effective fraction of ions that interact with the laser field, including any non-depleting background within the parent ion integration window, while the dimensionless parameter γ captures deviations from a purely single-photon response due to sequential absorption. The photon fluence is obtained from the measured pulse energy and the measured transverse beam profile at the interaction plane using an effective interaction area.

Results and discussion

Photo-uncaging of 2−OH and 3−OH

We find that $(\mathbf{2}-\mathrm{OH})^{1+}$ and $(\mathbf{3}-\mathrm{O}^{-})^{1+}$ undergo clean cleavage at the intended bond when irradiated by intense 355 nm laser light, as shown in Fig. 2A and C. Additional peaks are assigned to secondary fragments because they appear at higher fluence and increase thereafter, whereas the primary fragments decrease in the high-fluence regime (see Fig. 2B and D). The elemental composition after photo-induced dissociation is supported by high resolution mass spectrometry (HRMS) recorded after collision induced dissociation (CID) (see SI, pp. 19–31).

We find identical fragmentation patterns in CID and PID, as previously reported for multi-photon fragmentation of chromophore-tagged peptides.[30]

Fig. 2A, C and E show the 355 nm photocleavage mass spectra of $(\mathbf{2}-\mathrm{OH})^{1+}$, $(\mathbf{3}-\mathrm{O}^{-})^{1+}$, and $(\mathbf{3}-\mathrm{OH})^{2+}$, respectively. We observe a depletion of the parent peak by about 75–80%

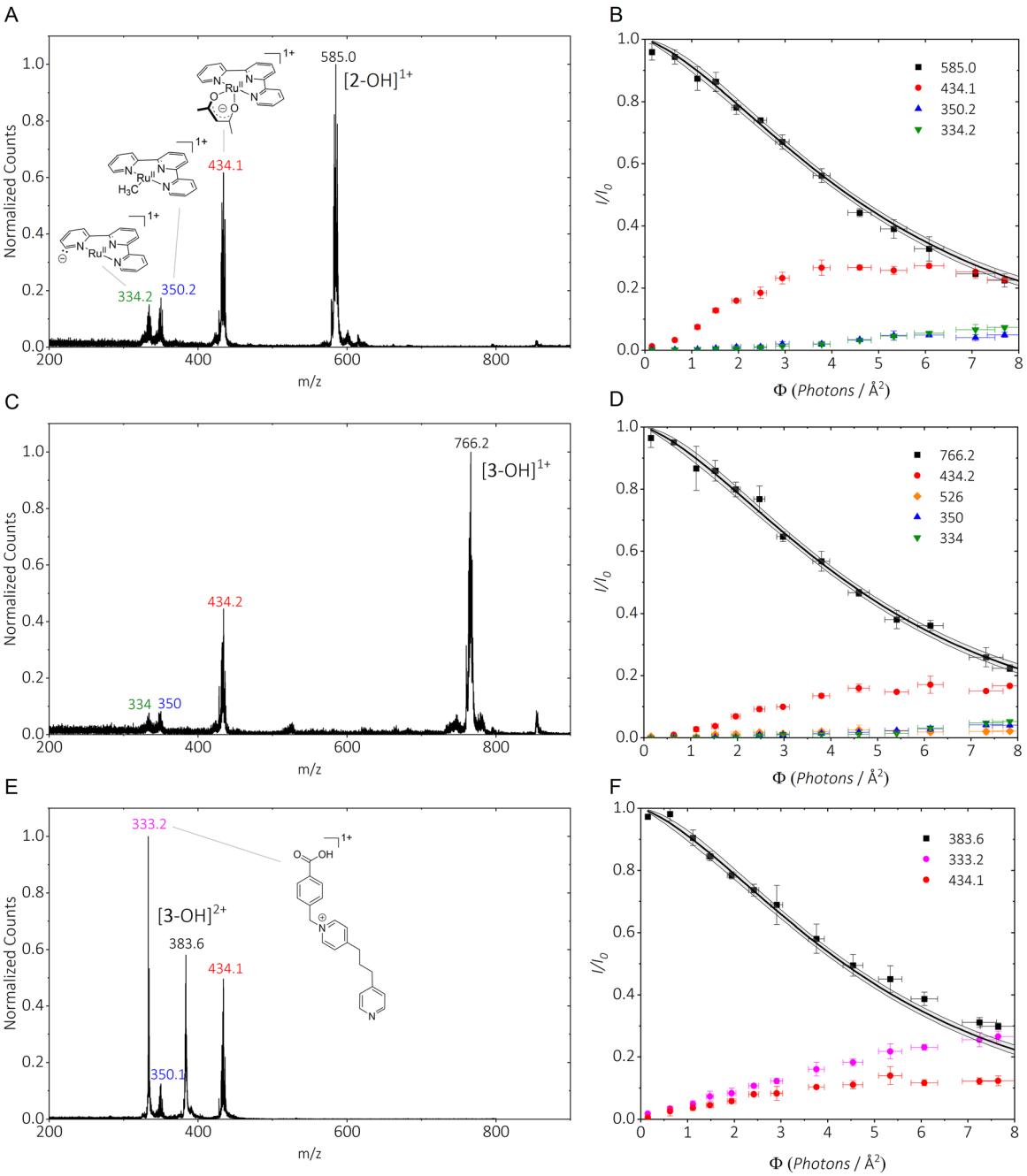

Fig. 2 Photolysis of **2** and **3**, by 355 nm laser light in high vacuum. (A) $(\mathbf{2}-\mathrm{OH})^{1+}$ releases a neutral pyridine, as witnessed by the appearance of the $[\mathrm{Ru(tpy)(acac)}]^{+}$ fragment at m/z = 434 Th. (C) $(\mathbf{3}-\mathrm{O}^{-})^{1+}$ likewise releases an overall neutral pyridine ligand. Panel (B) and (D) show photo depletion measurements of $(\mathbf{2}-\mathrm{OH})^{1+}$ and $(\mathbf{3}-\mathrm{O}^{-})^{1+}$ at 355 nm, respectively. Panel (E) shows the photolysis mass spectrum of $(\mathbf{3}-\mathrm{OH})^{2+}$ and Panel (F) the corresponding photodepletion measurement.

for all three compounds at a laser fluence of $\Phi \simeq 8$ photons Å^{-2}. Both, for $(\mathbf{2}{-}\mathrm{OH})^{1+}$ and $(\mathbf{3}{-}\mathrm{O}^{-})^{1+}$, photodissociation proceeds *via* neutral loss of the pyridinium ligand, as indicated by the appearance of $[\mathrm{Ru(tpy)(acac)(py)}]^{+}$ at m/z = 434. Depletion curves are well described by a predominantly sequential two-photon process with a small one-photon contribution ($1-\gamma \simeq 15-20\%$) and near-unity laser-ion beam overlap ($\alpha \simeq 95\%$), consistent with the very similar fit parameters obtained for all three species. A detailed fit yields photodepletion cross sections at 355 nm of $\sigma_{\mathrm{PD}} \simeq 3.5 \times 10^{-17}$ cm^2. Note that mass spectrometry reports the *photodepletion* cross section, *i.e.*, the product of the photoabsorption cross section and the cleavage yield under the present conditions.

The doubly charged $(\mathbf{3}{-}\mathrm{OH})^{2+}$ (m/z = 384) undergoes charge-separating fragmentation into two singly charged cations at m/z = 434 and 333 (Fig. 2E). The corresponding depletion curve (Fig. 2F) is likewise consistent with the same predominantly sequential two-photon response observed for the singly charged analogues, with fit parameters that fall within the ranges summarized above. Thus, while the charge state and molecular framework determine whether dissociation proceeds *via* neutral loss or charge separation, the overall photodepletion efficiency is primarily governed by the deposited photon energy and its intramolecular redistribution. In this context, the additional Coulomb energy in $(\mathbf{3}{-}\mathrm{OH})^{2+}$ (about 100 kJ mol^{-1}) appears minor compared with the ~674 kJ mol^{-1} delivered by absorption of two 355 nm photons.

Towards versatile photocages

The $[\mathrm{Ru(tpy)(acac)(L)}]^{+}$ motif with a pyridine leaving group was further modified by changing the position of the carboxylate group for bioconjugation. In complexes **2** and **3**, the biomolecule was attached to the leaving pyridine ligand, and the positive charge was removed with the dissociated ruthenium complex fragment after photofragmentation. In an alternative design, the protein is now linked to the tightly bound terpy–ligand, and a small charge-carrying pyridine leaving group is released upon photocleavage, while the ruthenium complex remains conjugated to the biomolecule. This design is more versatile because it allows for both the removal of negative charge from anions, such as $(\mathbf{4}{-}\mathrm{O}^{-})^{1-}$, and positive charge from cations, such as $(\mathbf{5}{-}\mathrm{O}^{-})^{1+}$ or $(\mathbf{5}{-}\mathrm{OH})^{2+}$. Exposure of the 1- charge state of the Ru(II) complex **4** to 355 nm laser light resulted in clean cleavage, accompanied by the release of the negatively charged 2-(4-pyridyl)ethane sulfonate ligand as intended (Fig. 3A). The 2+ charge state of complex **5** (m/z = 421) cleaved as expected to form a $[\mathrm{Ru(tpyderiv)(acac)}]^{+}$ (m/z = 554) and a benzylpyridinium (m/z = 289) fragment (see SI, Fig. S18). Exposure of the 1+ charge state (m/z = 842) of complex **5** to 355 nm light resulted, however, in the formation of a fragment at m/z = 554, while the expected benzylpyridinium fragment with m/z = 289 could not be detected (Fig. 3B).

The photolysis curves of both compounds show efficient cleavage that is consistent with sequential two-photon absorption, reaching cleavage probabilities above 80% at fluences of $\Phi \sim 7$ photons Å^{-2}. At 355 nm, the extracted photodepletion action cross sections for compound **4** agree in positive and negative ion mode, *i.e.* for $(\mathbf{4}{-}\mathrm{OH}+\mathrm{H})^{1+}$ and $(\mathbf{4}{-}\mathrm{O}^{-})^{1-}$, within their experimental uncertainties. In both cases, we obtain $\sigma_{\mathrm{PD}} \approx 6 \times 10^{-17}$ cm^2. Species $(\mathbf{5}{-}\mathrm{O}^{-})^{1+}$ and $(\mathbf{5}{-}\mathrm{OH})^{2+}$ show comparable photodepletion cross sections at 355 nm, $\sigma_{\mathrm{PD}} \approx 4 \times 10^{-17}$ cm^2.

Since solution phase UV-vis spectra of compounds **2–5** show substantially stronger absorption at 266 nm than at 355 nm, it is natural to extend the gas phase photo depletion measurements to 266 nm and to test whether the depletion mechanism (one- *vs.* sequential two-photon) changes with wavelength. Table 1 shows that, for every motif quantified at both wavelengths (positive ion mode), the extracted action cross section σ_{PD} is larger at 266 nm than at 355 nm. Within the quoted fit

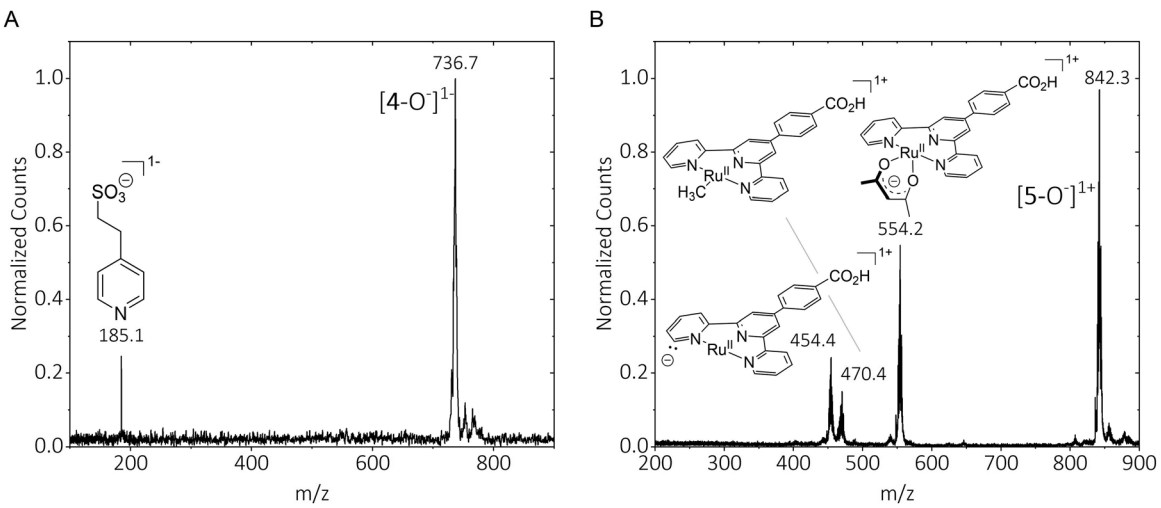

Fig. 3 Photolysis of the conjugates (**4**) and (**5**). (A) Irradiation of $(\mathbf{4}{-}\mathrm{O}^{-})^{1-}$ with 355 nm and Φ = 6 photons Å^{-2} leads to clean release of the negatively charged pyridine–sulfonate ligand in negative ion mode. (B) Irradiation of $(\mathbf{5}{-}\mathrm{O}^{-})^{1+}$ with 355 nm and Φ = 6 photons Å^{-2} in positive ion mode likely results in proton transfer from the pyridine–pyridinium ligand to the carboxylate of the tpy–ligand. The deprotonated pyridine–pyridinium ligand has been lost in the process and is not observable. Secondary fragments are formed under partial or full loss of the acac–ligand.

Table 1 Photo depletion fit parameters for species quantified at both wavelengths. Photo depletion cross sections σ_{PD} are given in units of 10^{-17} cm^2, and γ is given in %. The beam-overlap parameter α is not listed explicitly, it remains within 90–100% for all entries at both wavelengths

Motif	$\sigma_{PD}(355)$	$\gamma(355)$	$\sigma_{PD}(266)$	$\gamma(266)$
$(\mathbf{2}-OH)^{1+}$	3.7(4)	85(8)	7(1)	70(10)
$(\mathbf{3}-O^{-})^{1+}$	3.6(4)	80(10)	10(1)	80(10)
$(\mathbf{4}-OH + H)^{1+}$	6.3(3)	97(5)	13(2)	70(20)
$(\mathbf{5}-O^{-})^{1+}$	3.7(3)	91(7)	17(1)	95(5)

uncertainties this enhancement is unambiguous and the ratios $\sigma_{PD}(266)/\sigma_{PD}(355)$ span approximately ~2.0 up to ~4.5, with the largest increase observed for $(\mathbf{5}-O^{-})^{1+}$. Quantitative deviations from solution-phase absorption are expected because the measured action cross section $\sigma_{PD}(\lambda)$ can be written as the product of the absorption cross section $\sigma_{abs}(\lambda)$ and the dissociation quantum yield $\Phi_{diss}(\lambda)$, *i.e.* the fraction of excited molecules that dissociate after photon absorption. In UHV, the solvent-free environment can modify both σ_{abs} and Φ_{diss}, leading to a wavelength-dependent modulation of σ_{PD}. The fitted γ values provide a complementary, more mechanistic view. Although best fit γ decreases for some species at 266 nm (notably $(\mathbf{2}-OH)^{1+}$ and $(\mathbf{4}-OH + H)^{1+}$), these changes are comparable to the combined uncertainties and therefore do not constitute strong evidence for a qualitative shift in pathway. Overall, the data support a robust increase in photodepletion efficiency in the deep UV, while we do not find a systematic wavelength dependence in the relative one- *versus* two-photon contribution.

Photo-uncaging of oxytocin conjugates

In $[Ru(tpy)(acac)(L)]^{+}$ complexes, where L includes a peptide cargo such as oxytocin or insulin, the increased number of vibrational degrees of freedom is expected to accelerate intramolecular vibrational energy redistribution. Consistent with this expectation, CID studies generally find that larger biomolecules require higher internal energies to induce dissociation.[31]

To probe how increased molecular complexity affects the photocleavage response under otherwise identical beam and irradiation

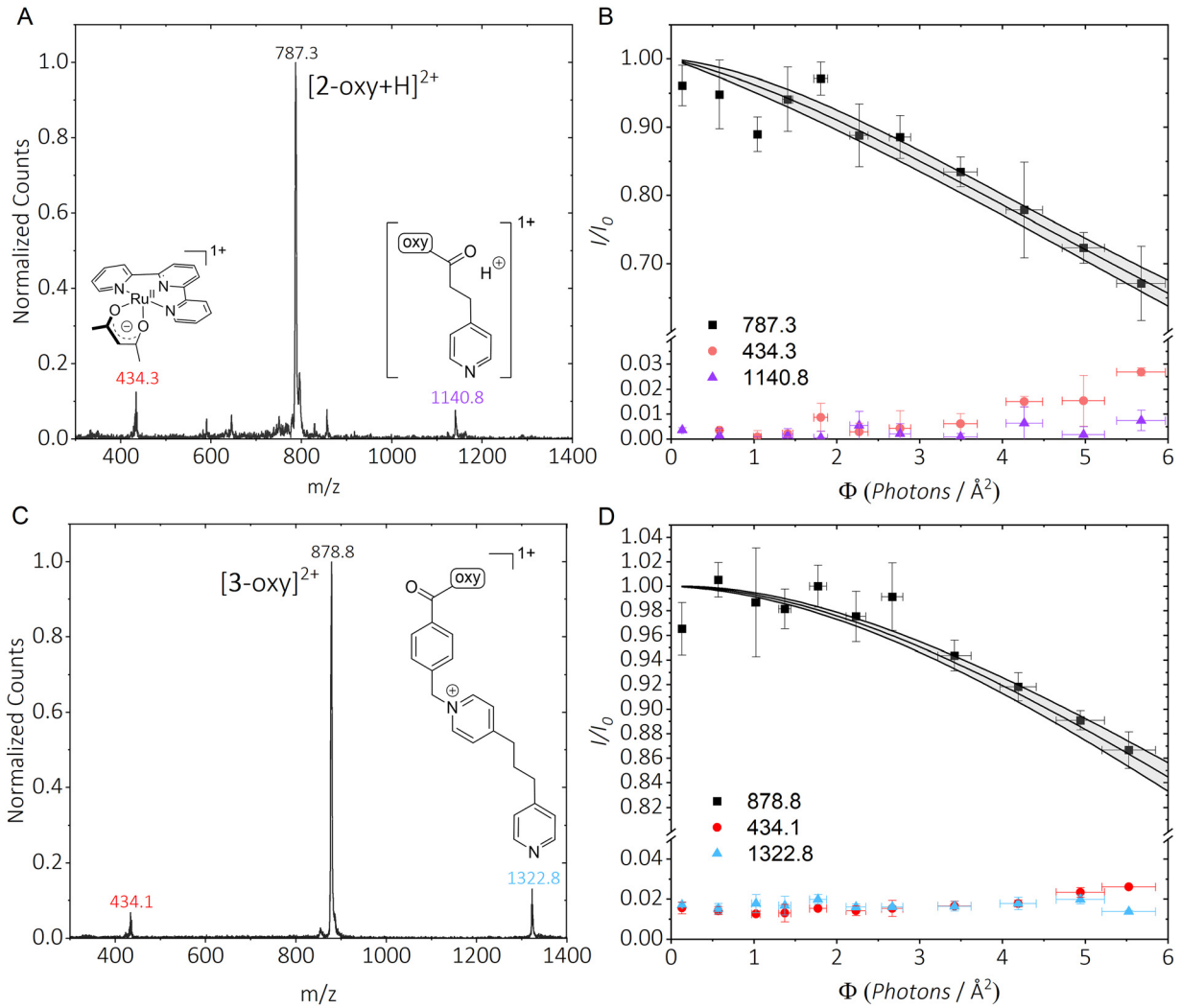

Fig. 4 (A) & (C) Mass spectra for photolysis of $(\mathbf{2}-oxy + H)^{2+}$ and $(\mathbf{3}-oxy)^{2+}$ at $\Phi > 8$ photons Å^{-2}. (B) & (D) UV photo depletion cross-sections for $(\mathbf{2}-oxy + H)^{2+}$ and $(\mathbf{3}-oxy)^{2+}$ with $\sigma_{PD} = (1.7 \pm 0.2) \times 10^{-17}$ cm^2 and $\sigma_{PD} = (1.2 \pm 0.1) \times 10^{-17}$ cm^2, respectively.

conditions, we conjugated chromophores **2** and **3** to the cyclic nonapeptide oxytocin and investigated both constructs in their doubly charged state, $(\mathbf{2}-\mathrm{oxy}+\mathrm{H})^{2+}$ and $(\mathbf{3}-\mathrm{oxy})^{2+}$. The corresponding singly charged conjugates $(\mathbf{2}-\mathrm{oxy})^{1+}$ and $(\mathbf{3}-\mathrm{oxy}-\mathrm{H})^{1+}$ exhibited parent depletion below the dynamic range of the accessible fluence series. The depletion curves in this regime do not provide sufficient curvature to extract stable values of γ and σ_{PD}, and we therefore do not report these species here.

Fig. 4A and C show the laser-induced fragmentation spectra of $(\mathbf{2}-\mathrm{oxy}+\mathrm{H})^{2+}$ and $(\mathbf{3}-\mathrm{oxy})^{2+}$. The corresponding parent survival curves are well described by the same sequential-absorption parametrization used throughout this work. Fits at 355 nm yield photodepletion action cross sections of $\sigma_{PD} = (1.7 \pm 0.2) \times 10^{-17}$ cm^2 for $(\mathbf{2}-\mathrm{oxy}+\mathrm{H})^{2+}$ and $\sigma_{PD} = (1.2 \pm 0.1) \times 10^{-17}$ cm^2 for $(\mathbf{3}-\mathrm{oxy})^{2+}$. For the same chromophore–linker motif, these values are reduced by roughly a factor of two to three compared with the corresponding peptide-free reference ions $(\mathbf{2}-\mathrm{OH})^{1+}$ and $(\mathbf{3}-\mathrm{O}^-)^{1+}$. This reduction indicates that conjugation to the peptide decreases the action efficiency for parent removal at fixed wavelength and fluence. Such a decrease is consistent with the larger manifold of competing relaxation channels and intramolecular energy flow pathways available in the peptide conjugates, which can reduce the probability that an absorption event leads to cleavage of the targeted bond within the experimental observation window.

The charge state further affects the observable depletion response. The inability to quantify $(\mathbf{2}-\mathrm{oxy})^{1+}$ and $(\mathbf{3}-\mathrm{oxy}-\mathrm{H})^{1+}$ within the available fluence range indicates that the corresponding action strength is substantially smaller for the monocations than for the dications. Because the parent depletion remains at the few-percent level in these cases, the extracted parameters are dominated by the low-fluence product $\alpha(1-\gamma)\sigma_{PD}$ and are particularly sensitive to systematic effects, which motivates their exclusion from the quantitative comparison.

Photo-uncaging of insulin conjugates

To demonstrate photo-uncaging on a protein and to test charge state control in a more complex cargo, we functionalized insulin at the N-terminus of the A-chain (Gly(A1)) with either **2** or **3**, yielding the conjugates **2**-ins and **3**-ins. In **2**-ins, an additional pyridinium unit was installed on Lys(B28) to provide a permanent remote charge (see SI).

Photodepletion mass spectra of these protein conjugates reveal similar fragmentation patterns and comparable relative fragment yields for **2**-ins and **3**-ins in a given charge state. Fig. 5 shows that irradiation produces a dominant, well-defined cleavage channel, indicating that the charge state of the protein conjugates can be controlled with high spatio-temporal selectivity.

Absolute action cross sections and absolute fragment yields could not be determined for the insulin conjugates. Under the available fluence parameter space in which the laser beam could be operated with a homogeneous flat-top profile, parent depletion remained below the level required for a reliable extraction of σ_{PD} and γ, and no robust depletion curves could be obtained. We therefore reduce the beam diameter to increase the peak intensity and acquired qualitative fragmentation spectra ($\Phi > 8$ photons Å^{-2}). These spectra reproduce the same fragment signatures across charge states and show only small charge dependent variations in relative intensities, supporting the conclusion that the overall charge state has a limited influence on the observed fragmentation pattern for the highly charged protein conjugates.

Conclusions

The experiments presented here demonstrate photo-uncaging and optical charge control of $[\mathrm{Ru(tpy)(acac)(L)}]^{n+}$ complexes in high vacuum, spanning small-molecule ligands as well as

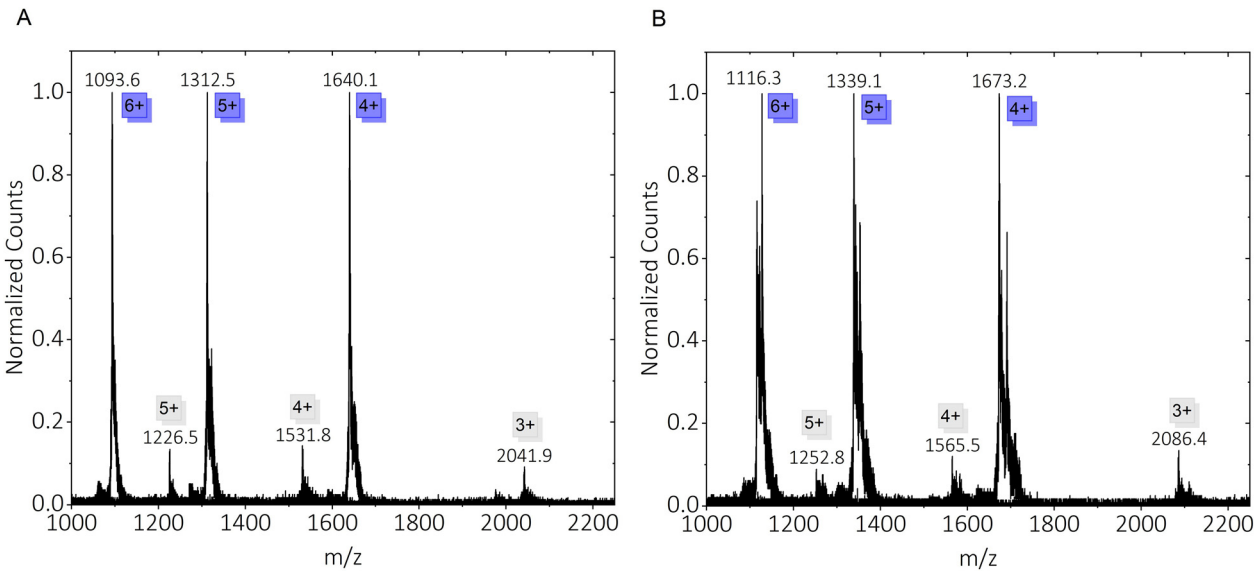

Fig. 5 Photocleavage mass spectra of insulin conjugates at 355 nm at $\Phi > 8$ photons Å^{-2}. (A) Mass spectra of $(\mathbf{2}-\mathrm{ins})^{n+}$ acquired for different initial charge states. (B) Mass spectra of $(\mathbf{3}-\mathrm{ins})^{n+}$ acquired for different initial charge states.

peptide and protein conjugates such as oxytocin and insulin. The data show that light-induced depletion of the parent signal is robust under UHV beam conditions and can therefore be used as an operational handle for beam manipulation and charge-state engineering.

For small reference motifs, substantial dissociation is already observed under 355 nm irradiation and the depletion response is consistently enhanced at 266 nm. The extracted photo depletion action cross sections are typically of order $\sigma_{PD} \sim 10^{-17}$ cm^2 at 355 nm and reach $\sigma_{PD} \approx 6 \times 10^{-17}$ cm^2 for the most efficient motifs. Measurements at 266 nm yield systematically larger action cross sections for every motif quantified at both wavelengths, including $(\mathbf{2}-\mathrm{OH})^{1+}$, $(\mathbf{3}-\mathrm{O}^-)^{1+}$, $(\mathbf{4}-\mathrm{OH} + \mathrm{H})^{1+}$, and $(\mathbf{5}-\mathrm{O}^-)^{1+}$, for which $\sigma_{PD}(266)$ increases into the range $(7\text{–}17) \times 10^{-17}$ cm^2.

These values provide a direct figure of merit for the net efficiency of the optically triggered depletion pathway under the experimentally relevant beam and timing conditions.

The extension of these measurements from small ligands to biomolecular cargoes shows that optical control at 355 nm remains accessible even for peptides and proteins. The observed depletion and charge-state changes for oxytocin and insulin establish that Ru-pyridyl-based tags can transfer optical addressability into the molecular-beam domain, where structured light fields can be used to reshape transmitted ensembles and to manipulate charge states with high spatio-temporal control.

Author contributions

Tag-design and synthesis: YH and AS. Chemical analysis: YH, VK and MP. Concept, funding, supervision: MA, MM and VK. Photocleavage design and experiments: MS and PG. Data analysis: YH, MS and VK. Writing of the manuscript: MS, VK and MA. Revision of the manuscript: all authors.

Conflicts of interest

There are no conflicts to declare.

Data availability

The data supporting this article have been included as part of the supplementary information (SI). Supplementary information: experimental setup of the high vacuum photolysis experiments, UV photodepeltion cross sections, synthesis and characterization of complexes and conjugates, CID-HRMS spectra, high vacuum photolysis spectrum of $(5\text{-OH})^{2+}$, NMR spectra. See DOI: https://doi.org/10.1039/d6cp00849f.

Acknowledgements

This work was supported in part by the European Union's Horizon 2020 research and innovation program under grant agreement # 860713 and by the Gordon & Betty Moore Foundation under grant number 10771. We acknowledge financial support from the Swiss National Science Foundation (SNF) (200020-207744). Open access funding was provided by Universität Wien/KEMOE. We thank Armin Shayeghi for supporting an early stage of the experiment. VK kindly thanks Thomas Ward and the Department of Chemistry at the University of Basel.

Notes and references

1 T. Šolomek, J. Wirz and P. Klán, *Acc. Chem. Res.*, 2015, **48**, 3064–3072.
2 T. Slanina, P. Shrestha, E. Palao, D. Kand, J. A. Peterson, A. S. Dutton, N. Rubinstein, R. Weinstain, A. H. Winter and P. Klan, *J. Am. Chem. Soc.*, 2017, **139**, 15168–15175.
3 R. Weinstain, T. Slanina, D. Kand and P. Klan, *Chem. Rev.*, 2020, **120**, 13135–13272.
4 D. Kand, L. Pizarro, I. Angel, A. Avni, D. Friedmann-Morvinski and R. Weinstain, *Angew. Chem., Int. Ed.*, 2019, **58**, 4659–4663.
5 A. R. Sekhar, Y. Chitose, J. Janos, S. I. Dangoor, A. Ramundo, R. Satchi-Fainaro, P. Slavicek, P. Klan and R. Weinstain, *Nat. Commun.*, 2022, **13**, 3614.
6 P. Klán, T. Šolomek, C. G. Bochet, A. Blanc, R. Givens, M. Rubina, V. Popik, A. Kostikov and J. Wirz, *Chem. Rev.*, 2013, **113**, 119–191.
7 J.-L. Fillaut, *Coord. Chem. Rev.*, 2024, **518**, 216050.
8 V. C. Cotham, Y. Wine and J. S. Brodbelt, *Anal. Chem.*, 2013, **85**, 5577–5585.
9 J. P. O'Brien, W. Li, Y. Zhang and J. S. Brodbelt, *J. Am. Chem. Soc.*, 2014, **136**, 12920–12928.
10 J. S. Brodbelt, *Chem. Soc. Rev.*, 2014, **43**, 2757–2783.
11 A. Theisen, B. Yan, J. M. Brown, M. Morris, B. Bellina and P. E. Barran, *Anal. Chem.*, 2016, **88**, 9964–9971.
12 J. B. Shaw, J. A. Madsen, H. Xu and J. S. Brodbelt, *J. Am. Soc. Mass Spectrom.*, 2012, **23**, 1707–1715.
13 L. J. Morrison and J. S. Brodbelt, *J. Am. Chem. Soc.*, 2016, **138**, 10849–10859.
14 J. R. Cannon, C. Kluwe, A. Ellington and J. S. Brodbelt, *Proteomics*, 2014, **14**, 1165–1173.
15 J. Schätti, M. Kriegleder, M. Debiossac, M. Kerschbaum, P. Geyer, M. Mayor, M. Arndt and V. Köhler, *Chem. Commun.*, 2019, **55**, 12507–12510.
16 M. Debiossac, J. Schätti, M. Kriegleder, P. Geyer, A. Shayeghi, M. Mayor, M. Arndt and V. Köhler, *Phys. Chem. Chem. Phys.*, 2018, **20**, 11412–11417.
17 Y. Hua, M. Strauss, S. Fisher, M. F. X. Mauser, P. Manchet, M. Smacchia, P. Geyer, A. Shayeghi, M. Pfeffer, T. H. Eggenweiler, S. Daly, J. Commandeur, M. Mayor, M. Arndt, T. Šolomek and V. Köhler, *JACS Au*, 2023, **3**, 2790–2799.
18 B. S. Howerton, D. K. Heidary and E. C. Glazer, *J. Am. Chem. Soc.*, 2012, **134**, 8324–8327.
19 J. D. Knoll, B. A. Albani, C. B. Durr and C. Turro, *J. Phys. Chem. A*, 2014, **118**, 10603–10610.
20 T. Naota, H. Takaya and S.-I. Murahashi, *Chem. Rev.*, 1998, **98**, 2599–2660.

21 M. J. Clarke, *Coord. Chem. Rev.*, 2003, **236**, 209–233.
22 P. B. Arockiam, C. Bruneau and P. H. Dixneuf, *Chem. Rev.*, 2012, **112**, 5879–5918.
23 L. Zeng, P. Gupta, Y. Chen, E. Wang, L. Ji, H. Chao and Z. S. Chen, *Chem. Soc. Rev.*, 2017, **46**, 5771–5804.
24 S. Bonnet, *J. Am. Chem. Soc.*, 2023, **145**, 23397–23415.
25 N. Toupin, S. J. Steinke, S. Nadella, A. Li, T. N. Rohrabaugh, Jr., E. R. Samuels, C. Turro, I. F. Sevrioukova and J. J. Kodanko, *J. Am. Chem. Soc.*, 2021, **143**, 9191–9205.
26 A. Li, C. Turro and J. J. Kodanko, *Chem. Commun.*, 2018, **54**, 1280–1290.
27 B. A. Albani, C. B. Durr and C. Turro, *J. Phys. Chem. A*, 2013, **117**, 13885–13892.
28 T. N. Rohrabaugh, Jr., A. M. Rohrabaugh, J. J. Kodanko, J. K. White and C. Turro, *Chem. Commun.*, 2018, **54**, 5193–5196.
29 M. N. Dunbar, S. J. Steinke, E. J. Piechota and C. Turro, *J. Phys. Chem. A*, 2024, **128**, 599–610.
30 M. Bouakil, A. Kulesza, S. Daly, L. MacAleese, R. Antoine and P. Dugourd, *J. Am. Soc. Mass Spectrom.*, 2017, **28**, 2181–2188.
31 J. M. Wells and S. A. McLuckey, *Methods Enzymol.*, 2005, **402**, 148–185.

